Erschienen in: Optical Materials Express ; 4 (2014), 4. - S. 575-586

Optical properties and birefringence in $LiInS_2$ in the terahertz frequency range

Shanpeng Wang,[1,2] Qijun Liang,[1,3,*] Xutang Tao,[2,3,4] and Thomas Dekorsy[1]

[1] *Department of Physics and Center for Applied Photonics, University of Konstanz, D-78457 Konstanz, Germany*
[2] *State Key Laboratory of Crystal Materials, Shandong University, 250100 Jinan, China*
[3]*These authors contributed equally to the paper.*
[4]*txt@icm.sdu.edu.cn*
[*]*qijun.liang@uni-konstanz.de*

Abstract: The birefringence of $LiInS_2$ (LIS) crystals in the THz frequency region is investigated by THz time-domain spectroscopy (THz-TDS). The experimental results indicate that LIS has large birefringence and low absorption in the THz frequency region. The optical properties of LIS are quantitatively determined. A sharp absorption caused by a TO-phonon resonance is observed at around 1.70 THz when the *Z*-axis is parallel to the polarization of the incident THz wave. A temporal separation of the transmitted THz pulses with different polarization components is realized by changing the orientation of the LIS crystal with respect to the polarization of the incident THz pulses. By controlling the relative phase and amplitude of the temporally separated THz pulses, THz polarization pulse shaping caused by birefringence in LIS crystal is demonstrated.

OCIS codes: (300.6495) Spectroscopy, terahertz; (160.4330) Nonlinear optical materials; (260.1440) Birefringence; (320.5540) Pulse shaping.

References and links

1. Y.-S. Lee, *Principles of Terahertz Science and Technology* (Springer, 2009).
2. Y. C. Shen, T. Lo, P. F. Taday, B. E. Cole, W. R. Tribe, and M. C. Kemp, "Detection and identification of explosives using terahertz pulsed spectroscopic imaging," Appl. Phys. Lett. **86**(24), 241116 (2005).
3. M. Nagel, P. H. Bolivar, M. Brucherseifer, H. Kurz, A. Bosserhoff, and R. Buttner, "Integrated THz technology for label-free genetic diagnostics," Appl. Phys. Lett. **80**(1), 154–156 (2002).
4. B. Fischer, M. Hoffmann, H. Helm, R. Wilk, F. Rutz, T. Kleine-Ostmann, M. Koch, and P. Jepsen, "Terahertz time-domain spectroscopy and imaging of artificial RNA," Opt. Express **13**(14), 5205–5215 (2005).
5. M. Tonouchi, "Cutting-edge terahertz technology," Nat. Photonics **1**(2), 97–105 (2007).
6. T. Löffler, T. Hahn, M. Thomson, F. Jacob, and H. Roskos, "Large-area electro-optic ZnTe terahertz emitters," Opt. Express **13**(14), 5353–5362 (2005).
7. J. T. Darrow, X. C. Zhang, and D. H. Auston, "Power scaling of large-aperture photoconducting antennas," Appl. Phys. Lett. **58**(1), 25–27 (1991).
8. D. You, R. R. Jones, P. H. Bucksbaum, and D. R. Dykaar, "Generation of high-power sub-single-cycle 500-fs electromagnetic pulses," Opt. Lett. **18**(4), 290–292 (1993).
9. S. Preu, G. H. Döhler, S. Malzer, L. J. Wang, and A. C. Gossard, "Tunable, continuous-wave terahertz photomixer sources and applications," J. Appl. Phys. **109**(6), 061301 (2011).
10. K. Kawase, Y. Ogawa, Y. Watanabe, and H. Inoue, "Non-destructive terahertz imaging of illicit drugs using spectral fingerprints," Opt. Express **11**(20), 2549–2554 (2003).
11. A. Dreyhaupt, S. Winnerl, T. Dekorsy, and M. Helm, "High-intensity terahertz radiation from a microstructured large-area photoconductor," Appl. Phys. Lett. **86**(12), 121114 (2005).
12. M. Jewariya, M. Nagai, and K. Tanaka, "Ladder climbing on the anharmonic intermolecular potential in an amino acid microcrystal via an intense monocycle terahertz pulse," Phys. Rev. Lett. **105**(20), 203003 (2010).
13. M. Liu, H. Y. Hwang, H. Tao, A. C. Strikwerda, K. Fan, G. R. Keiser, A. J. Sternbach, K. G. West, S. Kittiwatanakul, J. Lu, S. A. Wolf, F. G. Omenetto, X. Zhang, K. A. Nelson, and R. D. Averitt, "Terahertz-field-induced insulator-to-metal transition in vanadium dioxide metamaterial," Nature **487**(7407), 345–348 (2012).
14. Y. S. Lee, N. Amer, and W. C. Hurlbut, "Terahertz pulse shaping via optical rectification in poled lithium niobate," Appl. Phys. Lett. **82**(2), 170–172 (2003).
15. H. Wen and A. M. Lindenberg, "Coherent terahertz polarization control through manipulation of electron trajectories," Phys. Rev. Lett. **103**(2), 023902 (2009).

#201351 - $15.00 USD Received 19 Nov 2013; revised 17 Jan 2014; accepted 18 Jan 2014; published 3 Mar 2014

16. S. Fossier, S. Salaün, J. Mangin, O. Bidault, I. Thénot, J.-J. Zondy, W. Chen, F. Rotermund, V. Petrov, P. Petrov, J. Henningsen, A. Yelisseyev, L. Isaenko, S. Lobanov, O. Balachninaite, G. Slekys, and V. Sirutkaitis, "Optical, vibrational, thermal, electrical, damage, and phase-matching properties of lithium thioindate," J. Opt. Soc. Am. B **21**(11), 1981–2007 (2004).
17. S. Wang, Z. Gao, X. Yin, G. Liu, H. Ruan, G. Zhang, Q. Shi, C. Dong, and X. Tao, "Crystal growth and piezoelectric, elastic and dielectric properties of novel $LiInS_2$ crystal," J. Cryst. Growth **362**, 308–311 (2013).
18. S. Wang, H. Ruan, G. Liu, G. Zhang, Q. Shi, X. Zhang, Z. Gao, C. Dong, and X. Tao, "Growth, properties and first-principles study of mid-IR nonlinear optical crystal $LiInS_2$," J. Cryst. Growth **362**, 271–275 (2013).
19. S. Wang, X. Tao, C. Dong, Z. Jiao, and M. Jiang, "Growth of $LiInS_2$ single crystal by the accelerated crucible rotation technique," J. Synth. Cryst. **36**, 8–13 (2007).
20. L. Isaenko, I. Vasilyeva, A. Yelisseyev, S. Lobanov, V. Malakhov, L. Dovlitova, J. J. Zondy, and I. Kavun, "Growth and characterization of $LiInS_2$ single crystals," J. Cryst. Growth **218**(2-4), 313–322 (2000).
21. L. Isaenko, I. Vasilyeva, A. Merkulov, A. Yelisseyev, and S. Lobanov, "Growth of new nonlinear crystals $LiMX_2$ (M=Al, In, Ga; X=S, Se, Te) for the mid-IR optics," J. Cryst. Growth **275**(1-2), 217–223 (2005).
22. R. Gebs, G. Klatt, C. Janke, T. Dekorsy, and A. Bartels, "High-speed asynchronous optical sampling with sub-50fs time resolution," Opt. Express **18**(6), 5974–5983 (2010).
23. P. A. Elzinga, R. J. Kneisler, F. E. Lytle, Y. Jiang, G. B. King, and N. M. Laurendeau, "Pump/probe method for fast analysis of visible spectral signatures utilizing asynchronous optical sampling," Appl. Opt. **26**(19), 4303–4309 (1987).
24. A. Dreyhaupt, S. Winnerl, M. Helm, and T. Dekorsy, "Optimum excitation conditions for the generation of high-electric-field terahertz radiation from an oscillator-driven photoconductive device," Opt. Lett. **31**(10), 1546–1548 (2006).
25. G. Gallot and D. Grischkowsky, "Electro-optic detection of terahertz radiation," J. Opt. Soc. Am. B **16**(8), 1204–1212 (1999).
26. W. Zhang, A. K. Azad, and D. Grischkowsky, "Terahertz studies of carrier dynamics and dielectric response of n-type, freestanding epitaxial GaN," Appl. Phys. Lett. **82**(17), 2841–2843 (2003).
27. T. Ma, C. Yang, Y. Xie, L. Sun, W. Lv, R. Wang, C. Zhu, and M. Wang, "Electronic and optical properties of orthorhombic $LiInS_2$ and $LiInSe_2$: a density functional theory investigation," Comput. Mater. Sci. **47**(1), 99–105 (2009).
28. D. A. Roberts, "Simplified characterization of uniaxial and biaxial nonlinear optical crystals: a plea for standardization of nomenclature and conventions," IEEE J. Quantum Electron. **28**(10), 2057–2074 (1992).
29. G. Gallot, J. Zhang, R. W. McGowan, T.-I. Jeon, and D. Grischkowsky, "Measurements of the THz absorption and dispersion of ZnTe and their relevance to the electro-optic detection of THz radiation," Appl. Phys. Lett. **74**(23), 3450–3452 (1999).
30. Y. Ding and I. Zotova, "Second-order nonlinear optical materials for efficient generation and amplification of temporally-coherent and narrow-linewidth terahertz waves," Opt. Quantum Electron. **32**(4/5), 531–552 (2000).
31. K. Takeya, Y. Takemoto, I. Kawayama, H. Murakami, T. Matsukawa, M. Yoshimura, Y. Mori, and M. Tonouchi, "Terahertz generation and optical properties of lithium ternary chalcogenide crystals," J Infrared Milli Terahz Waves **32**(4), 426–433 (2011).
32. M. Schall, M. Walther, and P. Uhd Jepsen, "Fundamental and second-order phonon processes in CdTe and ZnTe," Phys. Rev. B **64**(9), 094301 (2001).
33. J. Hebling, G. Almasi, I. Kozma, and J. Kuhl, "Velocity matching by pulse front tilting for large area THz-pulse generation," Opt. Express **10**(21), 1161–1166 (2002).

1. Introduction

Terahertz (THz) radiation covers the frequency range from approximately 100 GHz to 10 THz [1]. It has attracted a considerable amount of interest over the recent decades due to its promising applications, such as medical imaging, security scanning, communication, industrial applications, and so on [2–5]. The key components for those applications are efficient THz sources and sensitive detection schemes. THz sources can be realized by optical rectification in nonlinear crystals [5, 6], photoconductive antennas (PCA) [7], magnetic field enhancement devices [8], and terahertz photomixing [9], etc. Electro-optic (EO) and photoconductive detection schemes are widely used for the detection of THz waves. THz time-domain spectroscopy (THz-TDS) [10] is one of the pivotal techniques to elucidate dynamic processes in the materials occurring on time scales of femtoseconds to picoseconds. It can be used in material science to study the complex dielectric response, birefringence and magneto/electro-optical effect in THz range. In THz-TDS systems, a broadband THz pulse is generated with a femtosecond laser pulse of typically 100 fs pulse duration in a photoconductive device [11]. This broadband THz pulse is detected with a delayed probe pulse in amplitude and phase after being transmitted through the sample. Besides THz

#201351 - $15.00 USD Received 19 Nov 2013; revised 17 Jan 2014; accepted 18 Jan 2014; published 3 Mar 2014

emitters and detectors other THz functional devices such as polarizing beam splitters, switchers, and filters are very important for THz technology. THz polarization-shaped waveforms are vital for THz spectroscopy and coherent control [12, 13]. THz wave shaping can be realized by using nonlinear optical crystals [14], and synthesizing THz waves with different polarizations [15].

$LiInS_2$ is one of lithium containing chalcogenide crystals and a lot of research has been done on its growth and physical properties [16–18]. It has large nonlinear optical (NLO) coefficients, a high laser damage threshold and a wide transparent wavelength range, which makes it an excellent mid-infrared NLO crystal. However, until now there is little research reported on its properties and applications in the THz frequency range.

In this paper, the birefringence properties of LIS crystals in the THz frequency region are investigated by THz-TDS. The basic optical constants in the frequency range of 0.4 - 2.2 THz, such as refractive indices and absorption coefficients are investigated. The experimental results reveal that LIS has a high transparency and a large birefringence over a large THz range, so they can be used as THz pulse splitters and pulse shapers. The phase difference and relative amplitude of the polarized waves can be controlled by changing the polarization of the incident THz wave with respect to the optical axis of LIS crystal. Furthermore, owing to its high transmission over the THz range, the waveforms of THz radiation can also be controlled by changing the crystal thickness.

2. LIS Crystal growth, experiment setup and theoretical model

The raw materials for the crystal growth of LIS were obtained from elementary Li (3N), In (5N) and S (5N) by a high temperature autoclave method [19]. Due to the high reactivity of lithium and the volatilization of sulfur, the stoichiometric ratio Li: In: Se of 1:1:2 was corrected, based on our experimental experience, to be 1.02:1:2.05. LIS crystals were grown using the synthesized materials in a pyrolytic boron nitride crucible by a modified Bridgman method [17, 18, 20, 21]. The axial temperature gradient is controlled to be 15 - 20 °C/cm at the growth interface in the furnace. The translation speed of the growth ampoule is 0.5 - 1 mm/h. After the charged crucible translated through the gradient zone completely, the furnace was cooled to room temperature at a speed of 30 °C/h. The LIS samples were cut from an integrated bulk LIS crystal along *a*-, *b*-, and *c*-axes, and were two-side polished for THz measurements.

The high-speed THz-TDS provides an excellent approach for the characterization of materials by measuring the absorption, transmission and reflection. In our THz-TDS experiments, a high-speed asynchronous optical sampling (ASOPS) system operates with mode-locked Ti:sapphire 1 GHz femtosecond oscillators as pump and probe lasers. One laser with repetition rate $f + \Delta f$ serves as the pump laser, the other with repetition rate f serves as the probe laser. In our experiments, the two pulsed lasers are stabilized to operate with a small repetition rate offset Δf of 2kHz using high-bandwidth feedback electronics [22]. ASOPS is a technique for ultrafast time-domain spectroscopy (TDS) without a mechanical delay stage [23], which provides excellent stability and sensitivity close to the shot noise limit. And the ASOPS system enables high scanning rates and a high time-resolution. The THz-TDS setup is schematically illustrated in Fig. 1. The pump pulse with an average power of 500 mW excites a large-area photoconductive THz emitter under normal incidence. The emitter is composed of an interdigitated finger structure with electrode width and spacing of approximately 5 μm on a GaAs substrate [11, 24]. The emitted THz pulse has linear polarization and is collected with a 90° off-axis parabolic mirror with 50.8 mm focal length. It is focused onto the sample with a spot of approximately 1 mm diameter by another parabolic mirror. The transmitted THz pulse is collimated and focused to a (110) ZnTe crystal of 500 μm thickness. The optical probe beam passing through a $\lambda/2$ wave plate with an average power of 350 mW overlaps with the THz spot on the ZnTe crystal through a hole in another off-axis parabolic mirror and detects the THz field induced transmission changes based on the electro-optic (EO) effect in

#201351 - $15.00 USD Received 19 Nov 2013; revised 17 Jan 2014; accepted 18 Jan 2014; published 3 Mar 2014

the ZnTe crystal [25]. The central wavelength and pulse duration of the pump and probe pulses are approximately 800 nm and 50 fs, respectively. The enclosure containing the THz beam path is purged with dry nitrogen gas to reduce the water absorption in ambient air. The transmitted probe pulse is focused onto the detector after propagating through a λ/4 wave plate and polarizing beam splitter cube (PBSC).

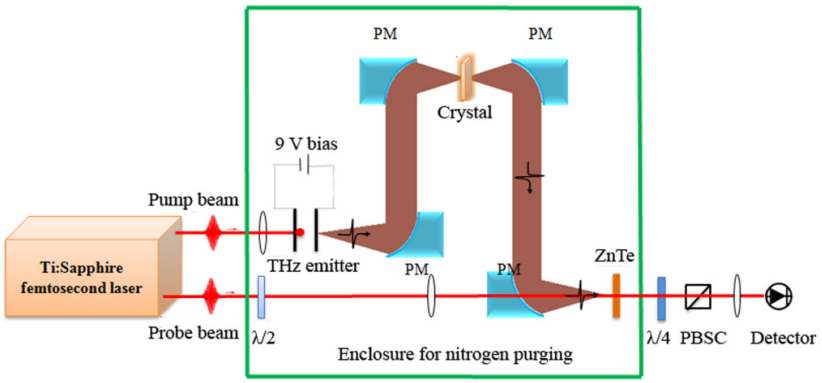

Fig. 1. Schematic sketch of the high-speed ASOPS THz-TDS setup.

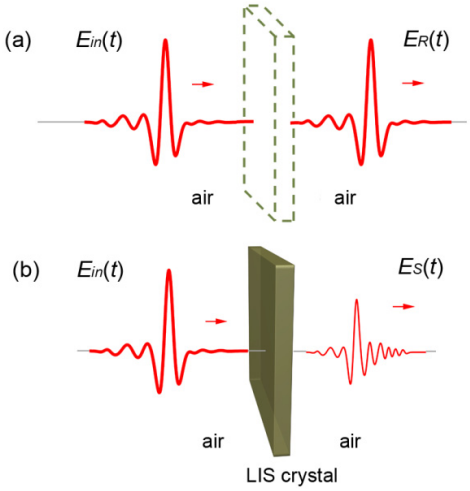

Fig. 2. Schematic sketch of electric field of THz waveforms with and without LIS crystal. (a) The reference waveform $E_R(t)$ measured without LIS. (b) The waveform $E_S(t)$ is measured after THz pulse passing through the sample.

The transmitted THz waveforms with and without LIS crystal are schematically shown in Fig. 2. The $E_{in}(t)$, $E_R(t)$, and $E_S(t)$ refer to the electric field of the incident THz pulse, reference, and THz pulse passing through the LIS, respectively. The transmitted time-domain electric field of the THz pulses through the air and LIS crystal are recorded with a 100-MS/s 14-Bit A/D converter (Gage CS8327: OCT-832-007), which is triggered by a cross-correlation signal between pump and probe laser generated by two-photon absorption in a GaP diode [22]. The phase-locked loop (PLL) feedback bandwidth is about 12 kHz. In addition, the scan time for a single measurement is 500 μs, which corresponds to the repetition rate offset Δf = 2 kHz between the pump and probe lasers. The corresponding frequency-domain spectra are obtained using numerical Fourier-transform (FT).

#201351 - $15.00 USD Received 19 Nov 2013; revised 17 Jan 2014; accepted 18 Jan 2014; published 3 Mar 2014

Considering a THz pulse propagating through a sample with complex refractive index $\tilde{n}_S(\omega) = n_S(\omega) + i\,\kappa_S(\omega)$ and thickness d, the complex transmission spectra of the reference and the sample can be expressed as [24]:

$$E_R(\omega) = E_{in}(\omega)\exp(ik_R d), \tag{1a}$$

$$E_S(\omega) = E_{in}(\omega)\frac{T_{as}T_{sa}\exp(ik_S d)}{1 + R_{as}R_{sa}\exp(2ik_S d)}, \tag{1b}$$

where R_{as}, R_{sa} and T_{as}, T_{sa} are the Fresnel reflection and transmission coefficients of the THz pulse propagating normally through air-sample and sample-air interfaces, respectively. $E_{in}(\omega)$ is the input frequency spectrum. $k_R(\omega) = \omega n_{air}(\omega)/c$ and $k_S(\omega) = \omega\tilde{n}_S(\omega)/c$ are the THz wave vectors through air and sample, respectively. Here we assume that $n_{air}(\omega) \equiv 1$, which indicates that the air has no dispersion in the studied frequency region.

There are subsequent "echoes" owing to the multiple reflections from the back and front sides of the sample and emitter. The main pulse and the echoes can be easily separated in the time domain. Therefore, the initial data analysis can be performed only on the main pulses [26]. For this simple case Eq. (1)b) can be simplified as:

$$E_S(\omega) = E_{in}(\omega)T_{as}T_{sa}\exp(ik_S d). \tag{2}$$

In the case of LIS, the imaginary part of refractive index is approximately 0.5% of the real part of the refractive index in the THz frequency range (see experimental results below). The assumption is additionally justified by theoretical consideration on the optical properties of LIS [27]. Hence, we obtain the complex amplitude ratio of the signals between the sample and reference.

$$\frac{E_S(\omega)}{E_R(\omega)} = A\exp(i\Phi) = \frac{4n_S(\omega)}{\left[n_S(\omega)+1\right]^2}\exp\left[-\alpha_S(\omega)d/2\right]\times\exp\left\{i\left[n_S(\omega)-1\right]\omega d/c\right\}, \tag{3}$$

where A is the amplitude and Φ the phase shift extracted from the Fourier transform. α_S denotes the power absorption coefficient of the sample. Comparing the amplitude ratio and phase shift between the sample and reference, the real part $n_S(\omega)$ of the refractive indices and the absorption $\alpha_S(\omega)$ of the sample can be obtained as follows:

$$n_S(\omega) = 1 + \frac{\Phi c}{\omega d}, \tag{4a}$$

$$\alpha_S(\omega) = -\frac{2}{d}\ln\left\{\frac{\left[n_S(\omega)+1\right]^2}{4n_S(\omega)}A\right\}. \tag{4b}$$

3. Birefringence property of LIS

LIS is a negative biaxial crystal in the optical wavelength range. The samples for measurements are *a*-, *b*- and *c*-cut LIS single crystals with different thickness. They were polished on the two opposite surfaces. In accordance with tradition, we use the capital letters *XYZ* for designation of the principal dielectric axes such that $n_X < n_Y < n_Z$ [28]. Since for LIS one has $n_b < n_a < n_c$ in optical wavelength range, the principal frame assignment will be $X \equiv b$, $Y \equiv a$, and $Z \equiv c$. The refractive index ellipsoid of LIS is expressed as:

$$\frac{X^2}{n_X^2} + \frac{Y^2}{n_Y^2} + \frac{Z^2}{n_Z^2} = 1, \tag{5}$$

#201351 - $15.00 USD Received 19 Nov 2013; revised 17 Jan 2014; accepted 18 Jan 2014; published 3 Mar 2014

where $n_X \neq n_Y \neq n_Z$. We firstly consider the sections of the normal surface by the three coordinate planes $x = 0$, $y = 0$ and $z = 0$ (xyz is the space coordinates system, as shown in Fig. 3).

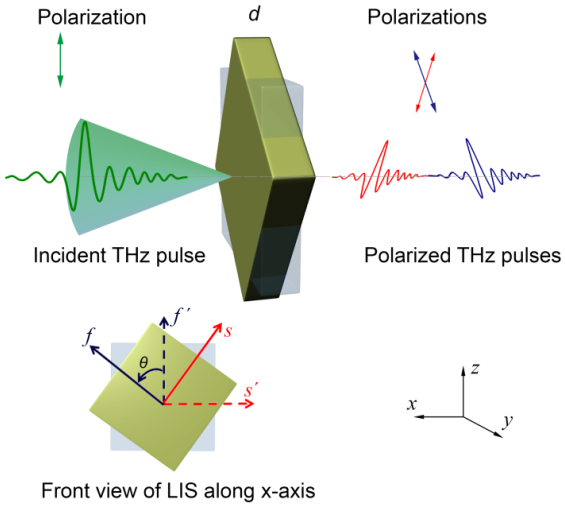

Fig. 3. Schematic of the polarizations of the THz pulses before and after propagating through the biaxial LIS crystal with the thickness of d along the x-axis. f, s and f', s' denote the polarizations of fast and slow THz pulses before and after crystal rotation, respectively. θ is the angle of crystal rotation. xyz is the space coordinates system.

The polarizations of incident and output THz pulses are shown in Fig. 3. The incident THz pulse is normal to the principal section of LIS crystal. The polarization of the incident pulse is along the z-axis. When neither of the two dielectric axes is parallel to the polarization of the incident THz pulse during the crystal rotation, the output pulse will be split into two sub-pulses in the time domain. The phase delay between fast and slow components is given by:

$$\Gamma = \omega d \Delta n / c, \tag{6}$$

where $\Delta n = n_s - n_f$ is the birefringence of the LIS crystal. And n_f and n_s are the fast and slow components of refractive indices, respectively. The phase retardation is proportional to frequency. When Γ is chosen properly, the crystal can be employed as a wave plate.

4. Results and discussion

4.1 LIS characterization using THz-TDS

In our experiments, we investigated LIS crystals which were cut along three crystallographic a-, b- and c-axes with different thickness. The corresponding transmitted time-domain THz waveforms and their spectra based on Fourier transform are shown in Fig. 4, Fig. 5 and Fig. 6, respectively.

#201351 - $15.00 USD Received 19 Nov 2013; revised 17 Jan 2014; accepted 18 Jan 2014; published 3 Mar 2014

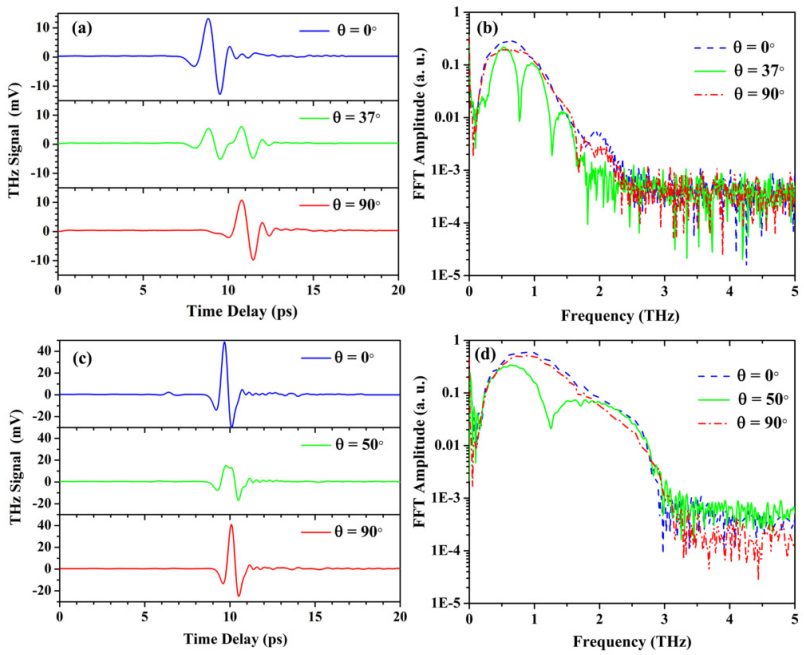

Fig. 4. (a) Transmitted time-domain THz pulses through *a*-cut LIS of 7.3 mm thickness with θ = 0°, 37°, 90°, respectively. (b) Frequency-domain spectra based on Fourier transform of (a). (c) Transmitted time-domain THz pulse through *a*-cut LIS of 0.65 mm thickness with θ = 0°, 50°, 90°, respectively. (d) Frequency-domain spectra based on Fourier transform of (c).

According to Eq. (6), the relative phases can be modulated by changing the thickness of samples. From the time-domain spectra of the transmitted THz waves, we can see that the waveforms can be modulated by changing the thickness of the crystal and the orientation of the crystal with respect to the polarization of the THz pulse. Figure 4(a) and Fig. 4(c) demonstrate phase changing by using *a*-cut LIS with different thickness of 7.3 and 0.65 mm. Figure 5(a) and Fig. 5(c) demonstrate phase changing by using *b*-cut LIS with different thickness of 5.0 and 0.70 mm. And Fig. 6(a) and Fig. 6(c) demonstrate phase changing by using *c*-cut LIS with different thickness of 6.5 and 0.50 mm.

#201351 - $15.00 USD Received 19 Nov 2013; revised 17 Jan 2014; accepted 18 Jan 2014; published 3 Mar 2014

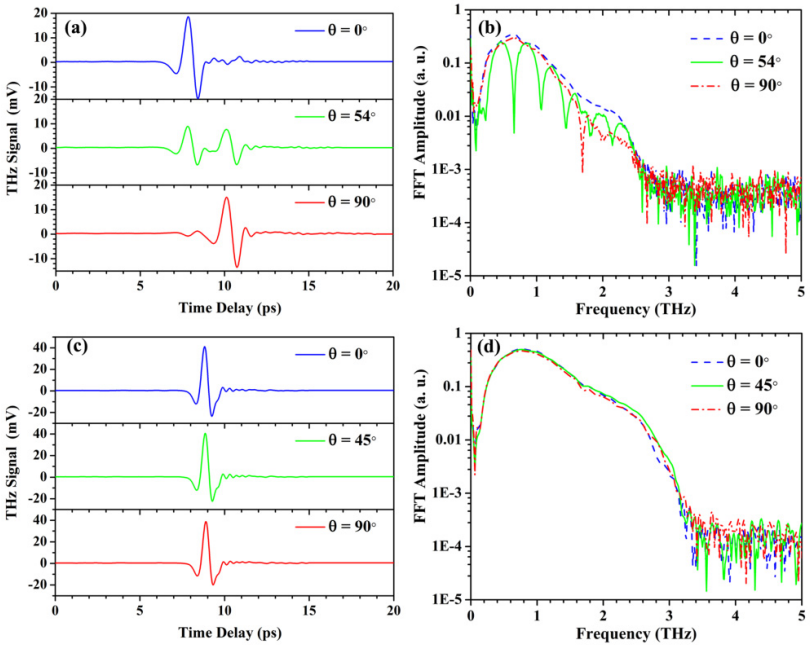

Fig. 5. (a) Transmitted time-domain THz pulses through *b*-cut LIS of 5.0 mm thickness with θ = 0°, 54°, 90°, respectively. (b) Frequency-domain spectra based on Fourier transform of (a). (c) Transmitted time-domain THz pulse through *b*-cut LIS of 0.70 mm thickness with θ = 0°, 45°, 90°, respectively. (d) Frequency-domain spectra based on Fourier transform of (c).

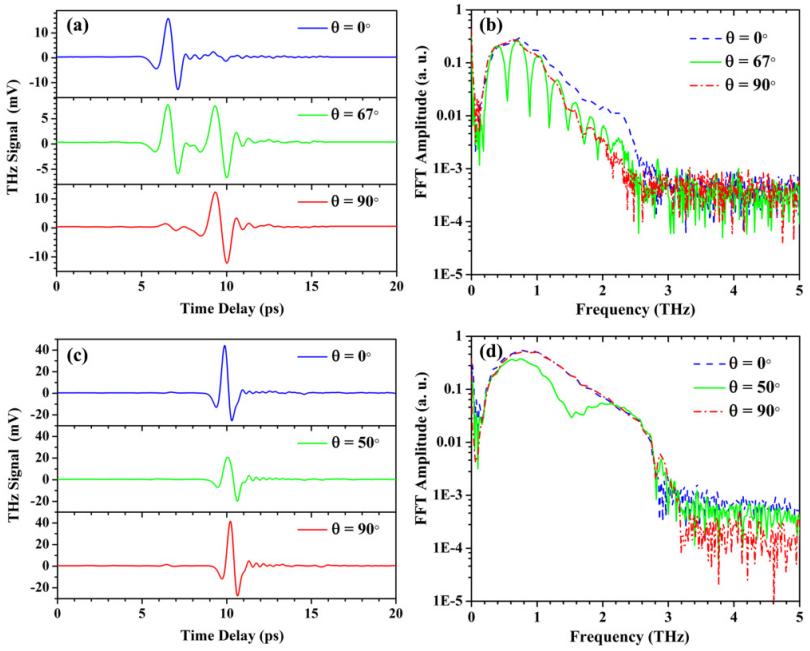

Fig. 6. (a) Transmitted time-domain THz pulses through *c*-cut LIS of 6.5 mm thickness with θ = 0°, 67°, 90°, respectively. (b) Frequency-domain spectra based on Fourier transform of (a). (c) Transmitted time-domain THz pulse through *c*-cut LIS of 0.50 mm thickness with θ = 0°, 50°, 90°, respectively. (d) Frequency-domain spectra based on Fourier transform of (c).

#201351 - $15.00 USD Received 19 Nov 2013; revised 17 Jan 2014; accepted 18 Jan 2014; published 3 Mar 2014

As mentioned above, we define $\theta = 0°$ when the THz pulse is polarized along the *f*-axis and $\theta = 90°$ when it is polarized along the *s*-axis. From the frequency-domain spectra of the transmitted THz waves, we can see a strong spectral modulation when θ is between 0° and 90°, which disappears when the polarization of the incident THz pulse is parallel to the *f*- or the *s*-axis. This strong modulation stems from the birefringence of the sample. Figure 4(a), Fig. 4(c), Fig. 5(a), Fig. 5(c) and Fig. 6(a), Fig. 6(c) demonstrate amplitude modulation by changing the orientations (θ) of *a*-, *b*-, and *c*-cut LIS with respect to the polarization of the THz pulse. For example in Fig. 4(a), we can continuously modulate the amplitudes of THz pulses by continuous changing the orientations (θ). However, we only choose three orientations (θ) to demonstrate the amplitude modulation. When $\theta = 0°$ or $\theta = 90°$, there is no pulse separation and amplitude modulation. When $\theta = 37°$, the strongest separation and modulation of the two THz pulse were demonstrated. For other orientations (θ), there are also modulations, but they are not the strongest ones. In a word, by controlling the relative phase and amplitude of the temporally separated THz pulses, THz polarization pulse shaping caused by birefringence in LIS crystal is demonstrated.

The pulse components polarized along the *f*- and *s*-axis travel at different velocities, which gives rise to a break-up of the single pulse into two separated pulses. The spectral modulation of the THz spectrum reflects the temporal separation of the two pulses. As is indicated in Fig. 6(a) and (b), the frequency spacing $\Delta\nu$ between two minima of 341.48 GHz corresponds to a time delay $\Delta\tau$ between the sub-pulses of 2.76 ps.

By calculating the complex amplitude ratio between the sample and reference spectra and using Eq. (4)a) and (4b), the refractive indices of the three dielectric axes can be obtained. Figure 7 illustrates the real part of refractive indices n_X, n_Y, and n_Z.

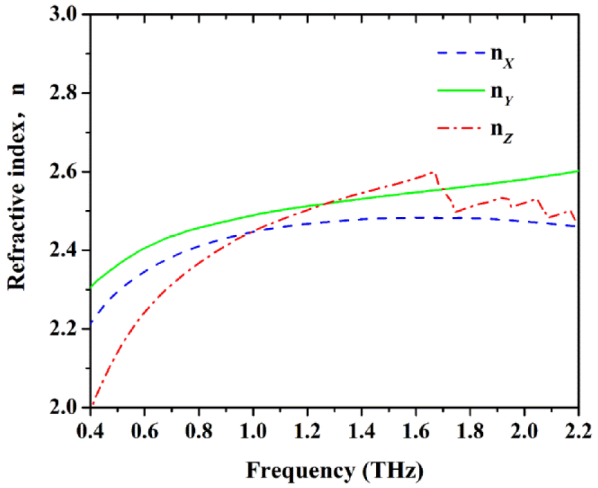

Fig. 7. The refractive indices of LIS crystal as a function of frequency along the three dielectric *X*-, *Y*-, and *Z*-axes.

In Fig. 7, n_X shows weaker frequency dependence than n_Y in the investigated THz frequency region. n_Z shows dispersive-like feature corresponding to a sharp absorption at a frequency around 1.70 THz, which will be discussed later. At the visible wavelength of 532 nm, the refractive indices of the three dielectric axes have been previously determined to be $n_X = 2.241$, $n_Y = 2.282$, $n_Z = 2.299$, respectively [15]. However, in the THz frequency region (1.5 THz, i.e. 200 μm), we determine the corresponding refractive indices to be 2.482, 2.539 and 2.564, respectively. With the knowledge of the refractive indices in the THz frequency range, the phase-matching conditions of LIS can be calculated, which is essential to realize the THz emission using LIS crystal.

#201351 - $15.00 USD Received 19 Nov 2013; revised 17 Jan 2014; accepted 18 Jan 2014; published 3 Mar 2014

The birefringence of LIS along *X*-, *Y*-, and *Z*-axes can be easily calculated from refractive indices n_X, n_Y, and n_Z of the three dielectric axes. The birefringence Δn along *X*-, *Y*-, and *Z*-axes are $n_Z - n_Y$, $n_Z - n_X$, and $n_Y - n_X$, respectively. The birefringence of LIS along *X*-, *Y*-, and *Z*-axes at the wavelength of 532 nm and 200 μm are shown in Table 1.

Table 1. The birefringence of LIS along *X*-, *Y*-, and *Z*-axes.

Wavelength	Birefringence, Δn		
	X-axis	*Y*-axis	*Z*-axis
532 nm	0.017	0.058	0.041
200 μm	0.025	0.082	0.057

As illustrated in Table 1, the birefringence in the THz region is larger than those in the visible region along the three orthogonal dielectric axes of LIS.

The E-O crystals such as GaAs, GaP, CdSe, $LiNbO_3$ and so on [29, 30] are widely used in THz technology due to their low absorption in the THz range. Their absorption coefficients are also no more than 10 cm^{-1} over the range of 0.4 - 2.2 THz. However, the absorption coefficient of $LiTaO_3$ is more than 100 cm^{-1}, which is two orders of magnitude larger than that of GaAs, GaP, CdSe, and $LiNbO_3$. The absorption coefficients α_X, α_Y, and α_Z are shown in Fig. 8. The absorption coefficients of LIS are mostly smaller than 10 cm^{-1} in 0.4 - 2.2 THz frequency range, which demonstrates relatively smaller THz absorption for LIS crystal. As mentioned above, a pronounced sharp absorption along the *Z*-axis can be observed at the frequency of 1.7 THz, which is the main origin of the dispersive feature of n_Z in Fig. 7. This absorption peak is attributed to a TO-phonon resonance along the *Z*-axis, which is also identified by Raman spectra in [15]. It is worth mentioning that there is no absorption feature in [31], which may be owing to the different LIS crystal samples. Additionally, the weak broad band absorption centered at 2.0 THz in α_Z and the second centered at 1.8 THz in α_X are observed. These broad band absorptions are probably caused by second-order phonon processes [32].

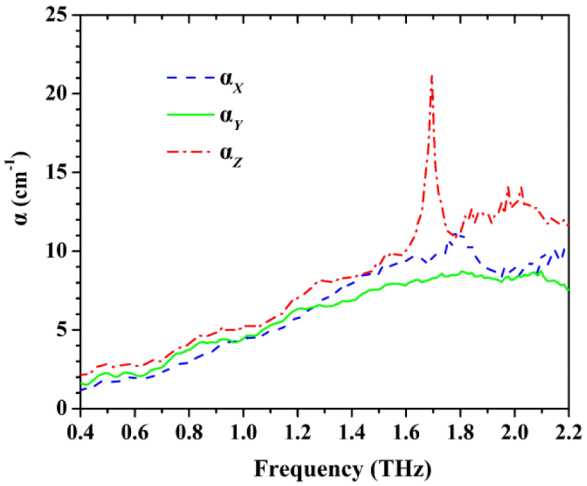

Fig. 8. Absorption coefficient of LIS crystal as a function of frequency at three dielectric *X*-, *Y*-, and *Z*-axes.

In Fig. 8, a slow absorption increase is observed over the frequency range of 0.4 - 2.2 THz. This increase is attributed to the low-frequency wing of TO phonons at higher frequencies [28]. From Raman spectroscopy a number of TO phonons are located in the frequency range from 3 to 10 THz [15]. The quantitative information on the optical properties

#201351 - $15.00 USD Received 19 Nov 2013; revised 17 Jan 2014; accepted 18 Jan 2014; published 3 Mar 2014

in the THz frequency range is important for applications in THz technology. Concerning LIS crystals, low absorption in combination with a second order optical nonlinearity $\chi^{(2)}$ of 16 pm/V [15] and the detailed knowledge of the phase matching condition allow for the generation of Terahertz radiation based on the concept of Hebling et al [33].

4.2. THz phase and amplitude modulation

As discussed before, LIS can be used as a wave plate and pulse shaper in the THz frequency range. The phase retardation between the *f*- and *s*-axes can be modulated by changing the orientation or the thickness of the crystal. From Fig. 4, Fig. 5 and Fig. 6, it is indicated that the transmitted THz pulse can be separated into two sub-pulses as the azimuth angle and the thickness of the crystal are chosen properly.

When the thickness of the crystal satisfies the condition $d > c\tau/\Delta n$ (c and τ are the light speed in vacuum and the THz pulse duration, respectively), the incident THz pulse can be separated completely after passing through the crystal when the polarization is not parallel or perpendicular to the dielectric axes.

For the investigated LIS crystals, the amplitude ratio of the fast and slow pulses can be adjusted by changing the azimuth angle of the crystal with respect to the polarization of the incident THz pulse. When the angle of the polarization of THz pulse with respect to *f*-axis is θ (as shown in Fig. 3), the electric field ratio between the fast and slow components after passing through the sample can be described below.

$$\frac{E_f(t)}{E_s(t)} = \frac{E(t,0)}{E(t,\pi/2)}\cot\theta. \tag{7}$$

where $E_f(t)$ and $E_s(t)$ are the transmitted time-domain THz electric field with polarization parallel to *f*- and *s*-axes, respectively. In Fig. 9, the relations of the time-domain amplitude ratio versus the azimuth θ are illustrated for the LIS crystals along *X*-, *Y*-, and *Z*-axes. Table 2 shows the angles when the two pulses have the same amplitude for the LIS crystals along *X*-, *Y*-, and *Z*-axes. When the two components have the same amplitude in the time-domain, a circular polarizer for THz wave can be fabricated.

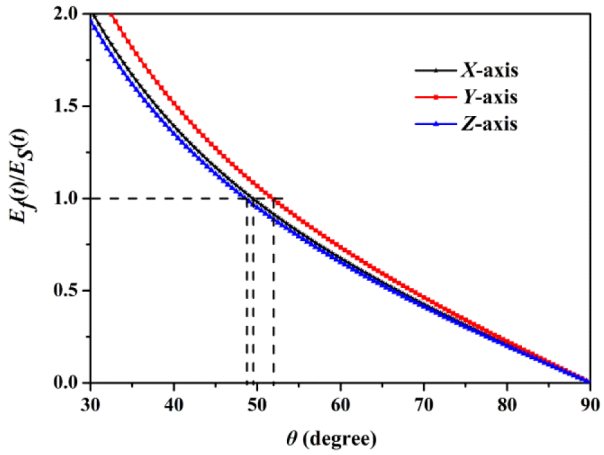

Fig. 9. Time-domain amplitude ratio $E_f(t)/E_s(t)$ as a function of the angle (θ) of the polarization of THz pulse with respect to *f*-axis.

#201351 - $15.00 USD Received 19 Nov 2013; revised 17 Jan 2014; accepted 18 Jan 2014; published 3 Mar 2014

Table 2. The angle (θ) of polarization with respect to *f*-axis when the amplitudes of the transmitted two components are equal.

	X-axis	*Y*-axis	*Z*-axis
θ (degree)	48.5	51.8	49.6

5. Conclusion

In conclusion, we have measured the optical properties of bulk LIS crystals in the THz frequency region of 0.4 - 2.2 THz by the THz-TDS. In the time-domain spectra, the phase separation and amplitude ratio of the two transmitted components were manipulated by changing the orientation of the crystal with respect to the polarization of the incident THz pulse and the crystal thickness. The birefringence of LIS crystal along the three dielectric axes in the THz range is larger than those in the visible range. Pronounced sharp absorption caused by a TO-phonon resonance is observed at around 1.7 THz when the *Z*-axis is parallel to the polarization of the incident THz wave. Due to its low absorption in the THz range, it is promising for LIS crystals to be fabricated as a circular polarizer, THz wave shaper, beam splitter, and wave plate. Crystal thickness can be additionally controlled continuously by applying an external electric field or changing the temperature of the crystal in a cryostat, which will be carried out in the future research.

Acknowledgments

We gratefully acknowledge the financial support from the Center for Applied Photonics (CAP) at the University of Konstanz, the DFG through the SFB 767 (Germany), the State National Natural Science Foundation of China (Grant No. 51272129, 51227002, 50721002) and the 973 Program of the People's Republic of China (Grant No. 2010CB630702). Thanks are also extended to China Scholarship Council (CSC).

#201351 - $15.00 USD Received 19 Nov 2013; revised 17 Jan 2014; accepted 18 Jan 2014; published 3 Mar 2014